Neutron scattering from fragmented frustrated magnets

F. Museur,[1,2] E. Lhotel,[1] and P. C. W. Holdsworth[2]
[1]*Institut Néel, CNRS and Université Grenoble Alpes, F-38042 Grenoble, France*
[2]*ENS de Lyon, CNRS, Laboratoire de Physique, F-69342 Lyon, France*

(Received 19 September 2022; revised 6 April 2023; accepted 17 May 2023; published 16 June 2023)

The fragmentation description is used to analyze calculated neutron scattering intensities from kagome ice and spin ice systems. The longitudinal, transverse, and harmonic fragments produce independent contributions to the neutron scattering intensity. This framework is used to analyze the ordering due to quantum fluctuations in the topologically constrained phase of kagome ice and the monopole crystal phase of spin ice. Here, quantum fluctuations are restricted to the transverse fragment, and they drive the system into a double-q structure in which longitudinal and transverse fragments have a different ordering wave vector. The intensity reduction of the Bragg peaks for the transverse fragments, compared with known classical limits, can be used as a diagnostic tool for quantum fluctuations. Published quantum Monte Carlo data for spin ice in a [111] field are consistent with the proposed protocol.

DOI: 10.1103/PhysRevB.107.214425

I. INTRODUCTION

Emergent gauge field descriptions [1] have revolutionized our vision of frustrated magnetism, leading us far from our expectations for microscopic systems. The monopole picture [2,3] of spin ice [4,5], the U(1) quantum spin liquid phase [6–9], and, more recently, the possible emergence of gauge fields of higher rank [10] are particularly remarkable examples. In spin ice this emergent description is a good approximation even at the microscopic level [11–14], so that the magnetic moments represent elements of a lattice field which, at low temperature and in zero external field, is the curl of an emergent gauge field, $\vec{A}$ [1,15]. This so-called "transverse" field leads to dipolar spin correlations in the low-temperature "Coulomb" phase [16]. The excitations of magnetic monopoles out of this monopole vacuum requires the syphoning off of a part of this magnetic flux reservoir to create an orthogonal, or "longitudinal," field, the gradient of a scalar potential Ψ. Application of an external magnetic field or the presence of surface charges requires a further separation giving the required harmonic field contribution [17,18], $\vec{h}$. This fragmentation of the magnetic resources [15,19] corresponds to a Helmholtz-Hodge decomposition [18] of the emergent vector field

$$\vec{M} = \nabla\Psi + \nabla\times\vec{A} + \vec{h}. \tag{1}$$

In this paper we explore the consequences of fragmentation for neutron scattering on spin-ice-like systems, concentrating on those in which quantum fluctuations are in competition with, or responsible for, the development of long-range magnetic order. In these systems, because of the separation in energy scales associated with the transverse and longitudinal fragments, quantum fluctuations are largely restricted to the transverse fragment. As a result, the fragmentation picture is extremely useful for the analysis. A characteristic of the ordered phases discussed is that the longitudinal and transverse fragments order with different wave vectors giving examples of "double-q" structures [20]. As our main example we concentrate on order driven from the "KII" phase, a topological liquid phase of kagome ice [21–23]. We show that, while the longitudinal fragment responsible for the charge orders in a $q = 0$ structure, the transverse fragment orders at a finite wave vector characteristic of the "dimer star phase" defined in detail below. The KII phase is generated in models of two-dimensional kagome ice that include long-range magnetostatic interactions and in the kagome spin planes lying perpendicular to an external field placed along the [111] direction in a spin ice material. Ordering out of the KII phase can be driven either classically by potential energy [21,22] or by quantum fluctuations in quantum spin models [24,25]. We make predictions for neutron scattering intensities from classical and quantum ordered states and compare them with published numerical data from quantum Monte Carlo simulations on quantum spin ice in a [111] field [25]. We also comment on the analogous three-dimensional system, the monopole crystal phase of quantum spin ice [26] in which a dense, ordered monopole structure would cohabit with a quantum spin liquid superposition of the transverse fragments.

The problems considered map onto dimer problems via their emergent field description [27]. In these phases, which show magnetic charge order, the transverse fragment maps exactly onto one of the Z_2 sectors of these emergent fields. The magnetic charge ordering explicitly breaks this Z_2 symmetry leaving a unique opportunity to observe dimer physics, quantum or classical, with a dipolar probe. That is, using neutron scattering within the dipole approximation, one can visualize the correlations emerging from the fictive quadrupolar objects.

The rest of the paper is organized as follows: In the next two sections we review the fragmentation picture for spin ice and its two-dimensional equivalent. In Sec. IV we show that neutron scattering data conveniently split into identifiable contributions from the transverse, longitudinal, and harmonic fragments. We illustrate this discussion using the low-temperature, "$\sqrt{3}\times\sqrt{3}$" phase of classical dipolar

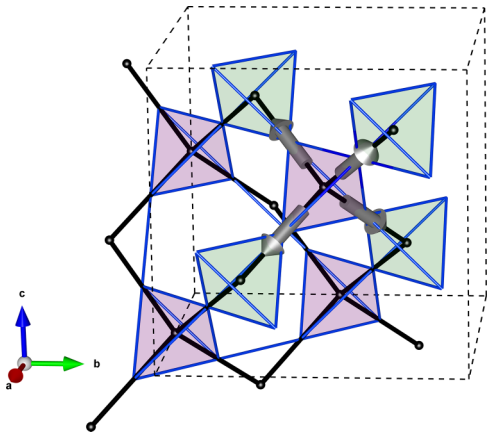

FIG. 1. Pyrochlore lattice (blue) and its dual diamond lattice (black). Tetrahedra of type A (B) are shown in shaded purple (green). The cubic unit cell is delimited by the dashed lines and contains 16 sites. The gray arrows show the four $\vec{d}_i$ vectors defined in the text.

kagome ice. In Sec. V we show how quantum fluctuations quantitatively change the predicted neutron scattering patterns as the classical phase changes to a quantum resonating phase and illustrate how this can be used as a diagnostic tool for detecting quantum fluctuations. In Sec. VI we relate our discussion to published quantum Monte Carlo data [25]. Section VII deals with the monopole crystal in spin ice, and the paper concludes with a general discussion. Throughout this paper we refer to the kagome plateau region of spin ice with an applied [111] field as the kagome plateau and to the two-dimensional problem of a single kagome plane of triangles as kagome ice.

II. A REVIEW OF FRAGMENTATION

Spin ice forms a pyrochlore lattice of corner-sharing tetrahedra, a four-sublattice face-centered cubic structure. The convention in discussing this system is to use an overlying cube of side a_c containing 16 sites, as shown in Fig. 1. A laboratory frame $[\hat{x}, \hat{y}, \hat{z}]$ is then defined with respect to the basis vectors of the cube. The spins take discrete orientations, pointing towards or away from the centers of the tetrahedra, along one of the four body diagonals of the cube: $\vec{S}_i = \pm\vec{d}_i$,

$$\vec{d}_1 = \frac{1}{\sqrt{3}}[-1,-1,1], \quad \vec{d}_2 = \frac{1}{\sqrt{3}}[1,-1,-1],$$
$$\vec{d}_3 = \frac{1}{\sqrt{3}}[-1,1,-1], \quad \vec{d}_4 = \frac{1}{\sqrt{3}}[1,1,1]. \tag{2}$$

At the microscopic level, the monopole picture corresponds to replacing the spins by needles carrying magnetic flux and therefore dumbbells [2,28] of magnetic charges into the centers of the tetrahedra. The tetrahedra form a diamond lattice of magnetic charge vertices, with a spin on each bond. The spins and diamond lattice sites are labeled i, j and I, J, respectively. The needles carry flux units of m/a, where m is the magnetic moment associated with the spin and $a = \frac{\sqrt{3}}{4}a_c$ is the diamond lattice constant. They can thus be considered as elements of a lattice field lying along the bonds of the diamond lattice: $M_{IJ} = (\vec{S}_i.\vec{d}_i)\frac{m}{a}\eta_I$. For the bipartite diamond lattice, $\eta_I = 1$ for a tetrahedron of type A, in which the out-pointing spin $\vec{S}_1$ falls along $\vec{d}_1$, and $\eta_I = -1$ for type B, which is the inverse. This convention ensures that $M_{IJ} = -M_{JI}$. These scalar elements can be converted into vector field elements by multiplying once again by the unit vector $\vec{d}_i$ lying on the bond IJ, $\vec{M}_{IJ} = M_{IJ}\vec{d}_i = -\vec{M}_{JI}$, which is proportional to the vector spin at the center of the bond.

The magnetic charge associated with each vertex is given by a discrete, on-lattice Gauss's law; $\sum_J M_{IJ} = -Q_I$, where the sum goes over the four nearest neighbors J to site I. The minus sign allows for the satisfaction of properties of both the emergent field and the real magnetostatic problem of spin ice [19]. The vertex charge takes values $Q_I = 0, \pm Q, \pm 2Q$, where $Q = 2m/a$ is the monopole charge [2]. Labeling the four field elements $[M_{IJ}]$ in order $1 \cdots 4$ [see Eq. (2)], a vertex satisfying the ice rule, with $Q_I = 0$ (two spins pointing in and two pointing out) can be written $[M_{IJ}] = [1, 1, -1, -1]$ in units of m/a. Using the same notation, monopole-carrying vertices are of the form $[M_{IJ}] = \pm[1, -1, -1, -1]$ for $Q_I = \pm Q$.

At this microscopic level, the Helmholtz-Hodge decomposition implies that each vertex set $[M_{IJ}]$ is cut into three distinct parts indicated by Eq. (1):

$$[M_{IJ}] = [M_{IJ}]_{\mathbf{m}} + [M_{IJ}]_{\mathbf{d}} + [M_{IJ}]_{\mathbf{h}}. \tag{3}$$

Here, **m** stands for monopole and represents the divergence-full longitudinal part, **d** stands for the divergence-free transverse part, and **h** stands for the harmonic contribution.

The decomposition can be calculated for any spin configuration by first identifying the vertices carrying magnetic charge and solving for the longitudinal field components via the Poisson equation [29]. Assuming periodic boundary conditions, the sum of the transverse and harmonic contributions is then the difference $[M_{IJ}] - [M_{IJ}]_{\mathbf{m}}$, which should satisfy Kirchoff's current law at each vertex. A more practical alternative method [30] iteratively calculates the divergence-free part $[M_{IJ}]_{\mathbf{d}} + [M_{IJ}]_{\mathbf{h}}$ for a given charge distribution, yielding $[M_{IJ}]_{\mathbf{m}}$ by the appropriate subtraction.

The harmonic contribution can be understood by considering the solution to Poisson's equation for charges distributed on a torus. It is invariant on adding a term $\psi'(\vec{r}) = \vec{h}\cdot\vec{r}$ to the scalar potential, with $\vec{h}$ being the spatially uniform harmonic field. As a consequence, multivalued solutions are analytically connected by winding a charged particle around the torus, returning to its starting position [29,31]. Winding a charge q along the $\hat{z}$ axis of a torus of scale L in dimension d would change $\vec{h}$ by $\delta\vec{h} \sim \frac{q}{L^{d-1}}\hat{z}$.

Moving these arguments directly to spin ice puts us on the diamond lattice of charge vertices with the cubic axes lying along the principal directions of the torus. The individual solutions correspond to different topological sectors [32] which fix the topological contribution to the magnetization. For simplicity, here we consider a situation with monopole concentration zero and magnetization maintained along the [001] direction either by an external field or by a symmetry-breaking perturbation [33]. The average magnetization per spin is then $\vec{M} = \frac{m}{\sqrt{3}}\epsilon\hat{z}$, from which we can identify a harmonic fragment for each field element of amplitude ϵ in units of m/a. For

any vertex lying on the A sublattice, the harmonic flux flows out along elements 1 and 4 and in through elements 2 and 3 [see Eq. (2)]:

$$[M_{IJ}]_h = \frac{m}{a}[\epsilon, -\epsilon, -\epsilon, \epsilon], \quad 0 \leqslant \epsilon \leqslant 1. \tag{4}$$

For a B sublattice the signs are reversed. As the magnetization becomes saturated, $\epsilon \to 1$ and the harmonic fragment takes on 100% of the magnetic resources.

The topological harmonic fragment remains defined even in the presence of a finite monopole concentration [29]. In this case, it will be dressed by a paramagnetic contribution to the magnetization due to the statistics of monopole configurations of finite extent. We choose to include this contribution as part of the longitudinal fragment, but both ultimately contribute to the magnetization and its fluctuations [32]. More realistic boundaries, with fixed surface charges and defects [34], will result in a harmonic component with some structure. Consequently, this will generate some diffuse scattering at finite $\vec{q}$ in addition to the topological contribution at $\vec{q} = 0$.

The topological sectors are isoenergetic (unlike for a standard fluid of electric charges [29]), but in zero field the sector straddling zero magnetization is selected entropically. As a consequence, in the monopole fluid phase, in zero external field, the harmonic contribution is zero to a good approximation, so that the field built from the magnetic moments decomposes into two "orthogonal" fluids with elements $[M_{IJ}]_{\mathbf{m}}$ and $[M_{IJ}]_{\mathbf{d}}$ [15].

As the monopole concentration goes to zero, only the transverse fragment survives, $[M_{IJ}] \to [M_{IJ}]_d$, while crossing the phase boundary into the all-in–all-out antiferromagnetic phase (a double monopole crystal [35,36]), the field elements are purely longitudinal, $[M_{IJ}] \to [M_{IJ}]_m$. The monopole crystal phase [15,37–40] is intermediate between these two limits [36] with $[M_{IJ}]$ divided evenly between $[M_{IJ}]_{\mathbf{m}}$ and $[M_{IJ}]_{\mathbf{d}}$. The monopole part forms long-range all-in–all-out order, and the dipolar part forms a Coulomb liquid with characteristic dipolar correlations.

III. FROM THE KAGOME PLATEAU OF SPIN ICE TO KAGOME ICE

Applying a magnetic field of modest strength along the [111] body-centered cubic axis aligns the apical spins of each tetrahedron along the field direction, as shown in Fig. 2. As the monopole concentration goes to zero, the system enters the kagome plateau region [41], in which kagome planes of spins lying perpendicular to the field direction enter the KII topological liquid phase with residual entropy at low temperature. In each tetrahedron the ice rules of two spins in and two out are satisfied, but as the apical spin is fixed to be out for an A tetrahedron and in for B, the three remaining spins in the in-plane triangles satisfy the kagome ice rule with two spins in and one out on an A triangle and two out and one in on a B triangle [42].

This evolution is well captured by fragmentation. A magnetic moment along the [111] axis can be decomposed into three cubic contributions of equal amplitude, each of which generates an independent harmonic fragment.

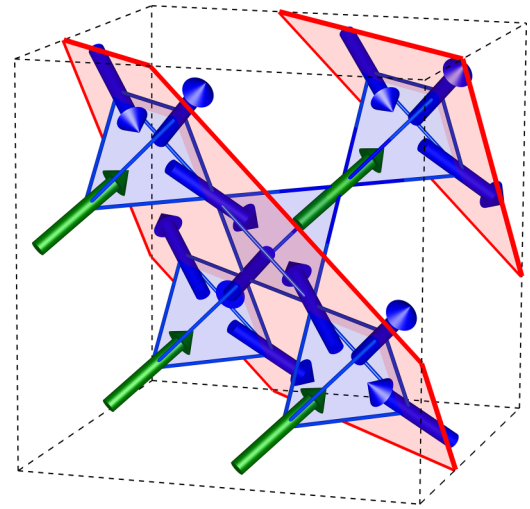

FIG. 2. Pyrochlore spin ice in a [111] field, showing the distinction between planes of pinned apical spins on a triangular lattice (green) and kagome planes satisfying the kagome ice rules (red).

Following Eq. (2), a vertex of type A has harmonic fragment

$$\begin{aligned}
[M_{IJ}]_h &= [M_{IJ}]_h^x + [M_{IJ}]_h^y + [M_{IJ}]_h^z, \\
[M_{IJ}]_h &= [-\epsilon, \epsilon, -\epsilon, \epsilon] + [-\epsilon, -\epsilon, \epsilon, \epsilon] + [\epsilon, -\epsilon, -\epsilon, \epsilon], \\
[M_{IJ}]_h &= [-\epsilon, -\epsilon, -\epsilon, 3\epsilon], \quad 0 \leqslant \epsilon \leqslant \tfrac{1}{3}.
\end{aligned} \tag{5}$$

The kagome plateau corresponds to $\epsilon = \frac{1}{3}$, so that for one of the three vertex configurations with spin 4 pointing along [111]

$$\begin{aligned}
[M_{IJ}] &= [-1, -1, 1, 1] \\
&= [0]_{\mathbf{m}} + \left[-\tfrac{2}{3}, -\tfrac{2}{3}, \tfrac{4}{3}, 0\right]_{\mathbf{d}} + \left[-\tfrac{1}{3}, -\tfrac{1}{3}, -\tfrac{1}{3}, 1\right]_{\mathbf{h}}.
\end{aligned} \tag{6}$$

The longitudinal fragment is zero, and the transverse fragment is restricted to the three spins in the plane with two elements of amplitude 2/3 and one of 4/3, which together satisfy Kirchoff's law. The harmonic term is identical for each tetrahedron or unit cell, spreading out evenly over the three in-plane spins. The apical spin is purely harmonic, and the sum over the contributions also satisfies the current law.

Spin ice fragmentation on the kagome plateau is intimately related to the fragmentation of two-dimensional spins in kagome ice. In this case the basic spin units are triangles whose centers form a honeycomb lattice of vertices for magnetic charge accumulation [15,21,22,43]. Considering the spins in an isolated kagome layer on the kagome plateau, the in-plane projection of the harmonic terms leaves a magnetic charge accumulation at the honeycomb lattice sites corresponding to the magnetic charge crystal observed in the KII phase of kagome ice [21,22]. The three-dimensional harmonic term therefore corresponds to a two-dimensional longitudinal term. Using a similar notation to the one used above, the two-dimensional three field elements entering a triangle of

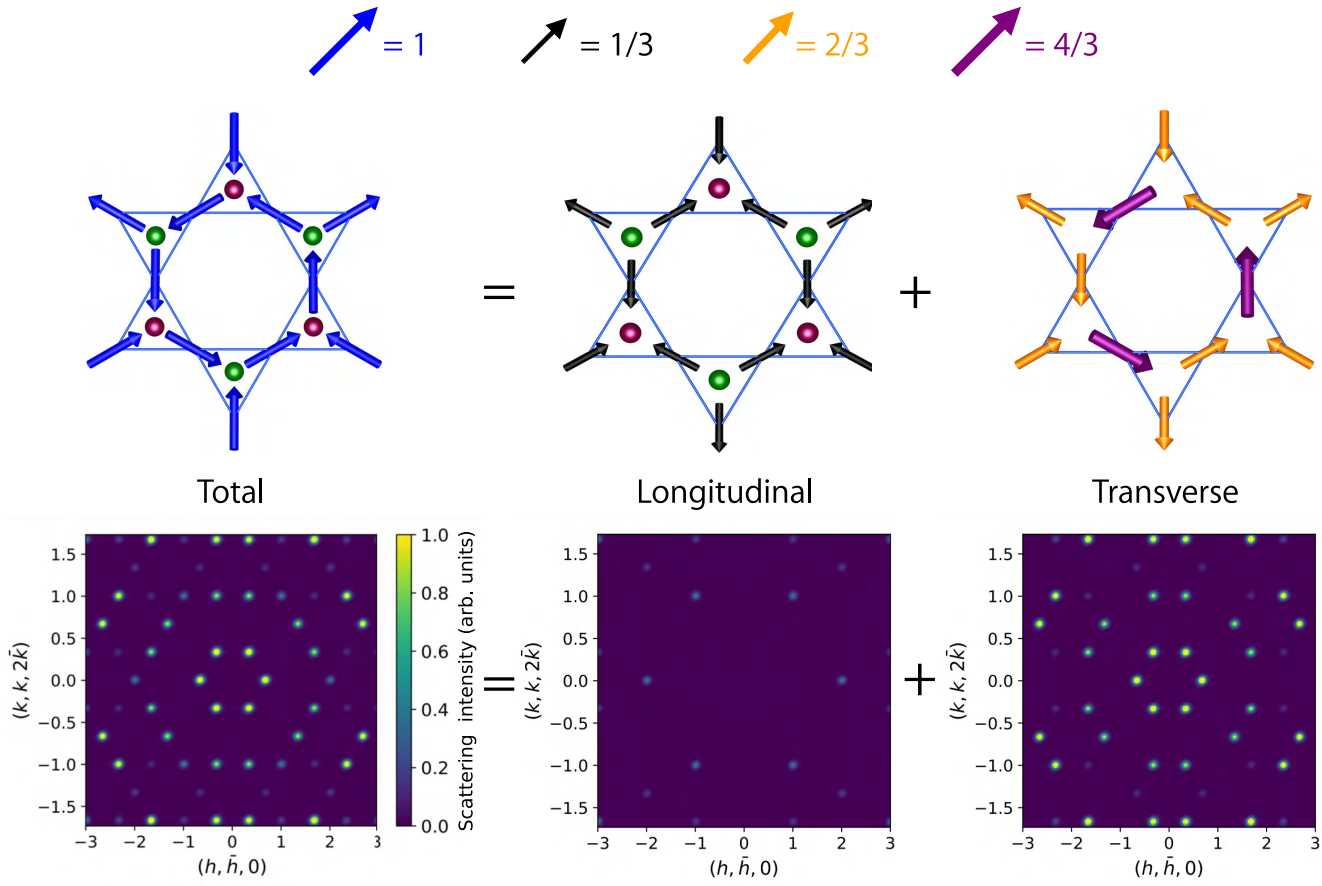

FIG. 3. Top: fragmentation of the $\sqrt{3}\times\sqrt{3}$ phase magnetic structure on a kagome plane. The magnetic unit cell extends over nine sites. Colors illustrate the amplitude of each component, and green and purple spheres show the placement of positive and negative magnetic charges within the dumbbell model. Left panel, full spin configuration. Middle panel, longitudinal fragment $\vec{M}_{\mathbf{m}}$ showing "all-spins-in–all-spins-out" ordering. Right panel, transverse fragment $\vec{M}_{\mathbf{d}}$ showing emergent ordering of the star phase. Bottom: SF neutron scattering intensities for neutrons polarized perpendicular to the plane computed from the total spin structure and the corresponding fragment above. The total scattering picture can also be computed by adding the separate intensities of the two fragments.

type A can be written

$$[M_{IJ}]^{\mathrm{2D}} = [-1,-1,1] = \left[-\tfrac{1}{3},-\tfrac{1}{3},-\tfrac{1}{3}\right]_{\mathbf{m}} + \left[-\tfrac{2}{3},-\tfrac{2}{3},\tfrac{4}{3}\right]_{\mathbf{d}} + [0]_{\mathbf{h}}. \quad (7)$$

The units of the field elements are $\frac{2m}{a\sqrt{2/3}}$, accommodating the projection of the three-dimensional spin vectors onto the plane [44], and the charge accumulation at the honeycomb vertices is only one-half of the in-plane monopole charge [2,45]. An example of such a decomposition is shown in Fig. 3 for the ordered $\sqrt{3}\times\sqrt{3}$ phase discussed in more detail in the next section.

IV. NEUTRON SCATTERING FROM FRAGMENTED STATES

The fragmentation decomposition is particularly useful for magnetic neutron scattering as the longitudinal and transverse fragments, when transformed into reciprocal space, are mutually orthogonal, while the topological harmonic fragment is restricted to wave vector $\vec{q} = \vec{0}$ and subsequent Brillouin zone centers. For a system of N spins the Fourier transform of a magnetic configuration is defined

$$\vec{M}(\vec{q}) = m \sum_{i=1,N} \vec{S}_i \exp(i\vec{q}\cdot\vec{r}_i) = a \sum_{I=1,N/4} \sum_{J=1,4} \vec{M}_{IJ} \exp\left(i\vec{q}\cdot(\vec{r}_I + \vec{\delta}_J)\right). \quad (8)$$

The spin and tetrahedron centers are at positions $\vec{r}_i$ and $\vec{r}_I$, respectively, and $\vec{\delta}_J = \frac{a}{2}\vec{d}_J$.

Following the spin fragmentation, we can write $\vec{M}(\vec{q}) = \vec{M}(\vec{q})_{\mathbf{m}} + \vec{M}(\vec{q})_{\mathbf{d}} + \vec{M}(\vec{q})_{\mathbf{h}}$. The component $\vec{M}(\vec{q})_{\mathbf{d}}$ is "transverse" in that it lies perpendicular to the wave vector $\vec{q}_* = \vec{q} - \vec{G}$, which is folded back into the first Brillouin zone by the appropriate reciprocal lattice vector $\vec{G}$. Both the "longitudinal" component, $\vec{M}(\vec{q})_{\mathbf{m}}$, and the harmonic component, $\vec{M}(\vec{q})_{\mathbf{h}}$, lie parallel to $\vec{q}_*$ with the latter restricted to the Brillouin zone centers.

Neutron scattering within the static approximation gives access to the Fourier transform of the two-site, one-time, spin-spin correlation function

$$S^{\alpha\beta}(\vec{q}) = \langle M_\alpha(\vec{q}) M_\beta(-\vec{q})\rangle, \quad (9)$$

where α, β are Cartesian indices x, y, z, $\vec{q}$ is the wave vector transfer of the scattering process, and $\langle \cdots \rangle$ represents a thermal average. The neutron scattering cross section is proportional to the projection of the correlation tensor perpendicular to $\vec{q}$

$$S(\vec{q}) = \langle |\vec{M}_{\perp}(\vec{q})|^2 \rangle, \tag{10}$$

where $\vec{M}_{\perp}$ is the projection of $\vec{M}$ perpendicular to $\vec{q}$. For simplicity we take the magnetic form factor to be a constant, independently of $\vec{q}$.

As a consequence of the orthogonality condition the structure factor also decomposes into distinct parts

$$S(\vec{q}) = S(\vec{q})_{\mathbf{m}} + S_{\mathbf{d}}(\vec{q}), \tag{11}$$

so that the scattering intensity divides into components from the divergence-full fragment (plus the harmonic fragment at the zone centers) and the divergence-free fragment of the magnetic moments with no interference terms. In the following sections we will demonstrate this property by computing the elastic scattering intensity of each fragment as well as of the total spin structure for different fragmented magnetic states. This property opens up the possibility of defining fragmentation order parameters by integrating the scattered intensity in specific regions of reciprocal space.

Inside the first Brillouin zone the scattering is purely transverse: $S(\vec{q}) = S_{\mathbf{d}}(\vec{q})$. For larger $\vec{q}$, as the scattering cross section lies perpendicular to $\vec{q}$ rather than $\vec{q}_*$, $S(\vec{q})$ develops contributions from the other two fragments. The separation of these fragments has already been observed in magnetic charge crystal phases [15,38,39,43,46]. In these phases the harmonic component can be ignored, the longitudinal fragment gives antiferromagnetic long-range order corresponding to the ordered array of magnetic charges, and the transverse part gives diffuse scattering characteristic of the Coulomb spin liquid phase [16].

In the case of polarized neutrons, $S(\vec{q})$ can be further resolved into "spin flip" (SF) and "non-spin-flip" (NSF) components corresponding to scattering events in which the neutron spin direction is flipped or not [14]. The SF scattering cross section lies in the plane perpendicular to the polarization axis and projects out the component of $\vec{M}_{\perp}(\vec{q})$ lying in this plane. The NSF component projects $\vec{M}_{\perp}(\vec{q})$ onto the polarization axis. This refinement leads to separate contributions to the structure factor, $S(\vec{q})^{\mathrm{SF}}$ and $S(\vec{q})^{\mathrm{NSF}}$, for scattering perpendicular and parallel to the polarization axis, each of which can be decomposed into the perpendicular fragmentation components. For an unpolarized source the measurement averages over all polarization directions leaving the total scattering intensity proportional to $S(\vec{q})$. Polarized neutron refinement is of particular interest for scattering from spin ice materials on the kagome plateau. In this case, choosing the neutron polarization along the [111] field direction allows for the resolution of spin components parallel and perpendicular to the kagome plane [44].

As a specific example we show the decomposition of the scattering intensity from a two-dimensional sample of kagome ice. A possible evolution of the classical KII phase, as the temperature is lowered, is to the "$\sqrt{3}\times\sqrt{3}$" phase, whose structure is illustrated in the top panels of Fig. 3 [21,22]. The repetition distance for the unit cell is $\sqrt{3}$ larger than that of the kagome lattice. As shown, the spins in the unit cell can be fragmented. The longitudinal part gives the charge order of alternate positive and negative charges, with a reduced unit cell of three sites. The transverse part maintains the nine-site unit cell, whose configuration maps onto the emergent field of a dimer solid, the "star phase" in which a tiling of the unit cells produces three distinct types of hexagonal ring. One out of the three types of hexagon forms a sixfold-symmetric star of dimers, from which the phase takes its name [47,48]. The longitudinal, transverse, and total contributions to the scattering intensity from this ordered state are shown in the bottom panels of Fig. 3. For the kagome plateau of spin ice, this in-plane scattering intensity would correspond to $S(\vec{q})^{\mathrm{SF}}$ with the neutron source polarized along the [111] direction. In this case the longitudinal fragment corresponds to the projection onto the plane of the three-dimensional harmonic component, which is channeled out of each tetrahedron via the apical spin (not included) [44] [see Eqs. (6) and (7)]. The data are shown in the scattering plane of the kagome lattice in units appropriate for spin ice and the kagome plateau: the in-plane axes $[k, k, 2\bar{k}]$, $[h, \bar{h}, 0]$ lie perpendicular to the [111] field axis and are in units of $2\pi/a_c$. The sixfold symmetry of the spins lying in the plane is represented in the figure by scaling the $[k, k, 2\bar{k}]$ axis by a factor of $\frac{1}{\sqrt{3}}$.

This analysis shows that rather surprisingly, this simplest of phases, the classical $\sqrt{3}\times\sqrt{3}$ phase, is a fragmented double-q structure whose scattering pattern is the sum of intensities from the longitudinal and transverse parts. These fragments have different ordering wave vectors and have no communal Bragg peaks, so that the total scattering is made up of resolvable contributions from the charge ordering and the emergent field from the star phase. The charge ordering from the longitudinal component corresponds to antiferromagnetic, "all-spins-in–all-spins-out" order. This is a "$\vec{q} = 0$" order, with Bragg peaks at the centers of the kagome lattice Brillouin zone starting at $h = 2$, $k = 0$ and symmetry-related points, the scattering intensity being zero at the zone centers with smaller wave vector transfer. The star phase from the transverse component shows Bragg peaks at $h = \frac{2}{3}$, $k = 0$ and symmetry-related points. These correspond to the basis vectors of the reciprocal space for the $\sqrt{3}\times\sqrt{3}$ unit cell with magnitude $q = \frac{2\pi}{a_c}(\frac{2\sqrt{3}}{3})$. Peaks at larger q repeat in a distinctive, sixfold-symmetric pinwheel pattern which we can take to be characteristic of the star phase.

V. QUANTUM FLUCTUATIONS: THE SPIN-*P* AND PLAQUETTE PHASES

In this section we consider the effect of quantum fluctuations on the KII phase of kagome ice. It is known that quantum fluctuations driven by a small transverse spin component could drive the spins into a partially ordered phase at low temperature [23–25]. In this resonating $\sqrt{3}\times\sqrt{3}$ phase, which we refer to as the spin-*P* phase, two of the three types of hexagonal spin arrangement provide a framework for resonating loops of six spins around the third class of hexagon. This quantum resonance corresponds to a linear superposition of the two states per unit cell with spin rotations around the enclosed hexagon in opposite directions, leaving an effective

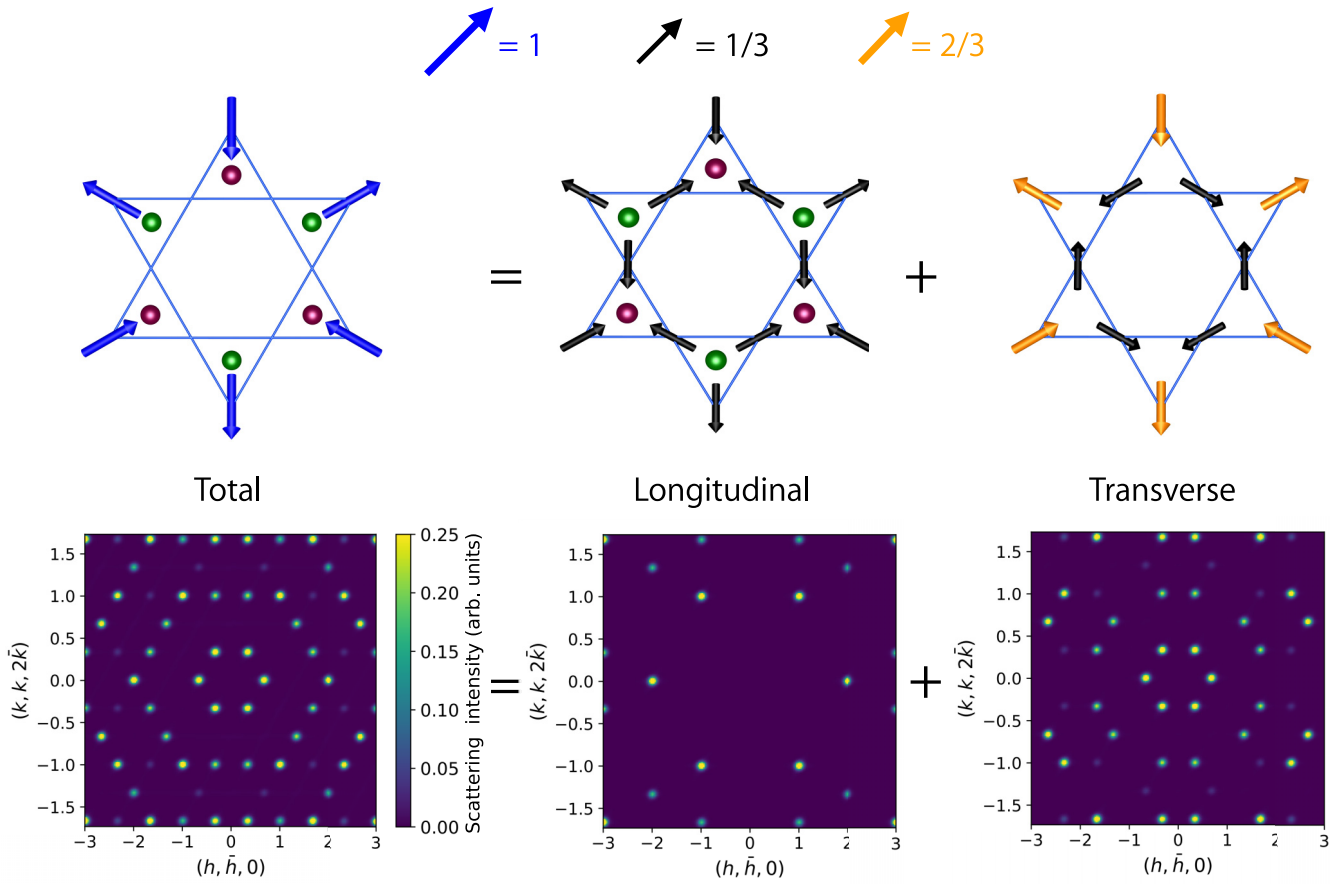

FIG. 4. Top: fragmentation of the spin-P phase magnetic structure on a kagome plane. The magnetic unit cell extends over nine sites. Colors illustrate the amplitude of each component, and green and purple spheres show the placement of positive and negative magnetic charges within the dumbbell model. Left panel, full spin configuration. The quantum resonance on the hexagonal loop results in the effective absence of spins around the loop. Middle panel, longitudinal fragment $\vec{M}_{\mathbf{m}}$ showing "all-spins-in–all-spins-out" ordering. Right panel, residual transverse fragment $\vec{M}_{\mathbf{d}}$ corresponding to the residual emergent field of the dimer plaquette phase (see top panel of Fig. 5). Bottom: SF neutron scattering intensities for neutrons polarized perpendicular to the plane computed from the total spin structure and the corresponding fragment above. The total scattering picture can be computed by adding the separate intensities of the two fragments. Note that the absolute intensity scale is one-quarter of that in Fig. 3.

magnetic state with reduced total moment, as shown in the top left panel of Fig. 4.

To show that the spin-P phase corresponds to the coexistence of the classical charge ordered phase and an emergent quantum dimer phase [47,48], one must first apply the fragmentation procedure to the effective reduced moments once the quantum spin resonances have been taken into account. From the top panels of Fig. 4, one can see that the residual spin on each triangle can be written, using the previous notation, as $\pm[-1, 0, 0]$, arranged such that the charge order is preserved. A vertex carrying a positive charge can thus be fragmented into a longitudinal and a transverse part

$$[-1, 0, 0]=\left[-\tfrac{1}{3}, -\tfrac{1}{3}, -\tfrac{1}{3}\right]_{\mathbf{m}} + \left[-\tfrac{2}{3}, \tfrac{1}{3}, \tfrac{1}{3}\right]_{\mathbf{d}} + [0]_{\mathbf{h}}. \qquad (12)$$

This decomposition confirms that, on driving the $\sqrt{3}\times\sqrt{3}$ phase into the spin-P phase with quantum fluctuations, the charge ordering and hence the longitudinal fields are unchanged, while the amplitude of the transverse part is reduced by a factor of 2. The quantum resonance is therefore limited to the transverse fragment as announced. In dimer language, adding quantum fluctuations to the star phase leads to resonating closed loops of dimers, which can lead to a quantum phase transition to the "plaquette phase." This is not a liquid phase, as dimer translational symmetry remains broken such that resonances are limited to plaquette flips of dimers around one of the three types of hexagon of the star phase. The corresponding resonance of the emergent field for the dimers is shown in the top panel of Fig. 5. Similarly to the residual spin of the spin-P phase, it is constructed as the average of both emergent field configurations around a plaquette. Despite the resonance, the field retains a static residue which is precisely that of the transverse spin fragment shown in Eq. (12). The spin-P phase is therefore a superposition of the charge ordered phase and the dimer plaquette phase represented by a single Z_2 sector of its emergent field.

In the simplest quantum dimer models, quantum fluctuations are generated through off-diagonal couplings between classical configurations that generate the hexagonal plaquette flips of dimers [47,48]. The off-diagonal energy scale, g, is in competition with a classical, three-body interaction term, μ, giving an energy scale for a three-dimer hexagon and an

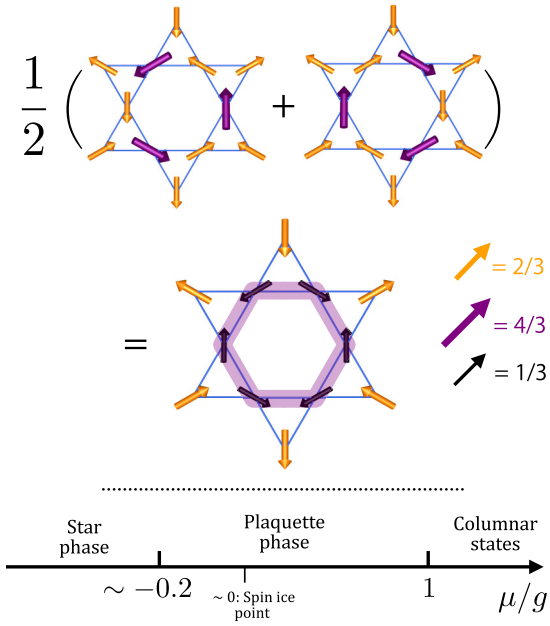

FIG. 5. Top: the quantum resonance of the emergent field for dimers in the plaquette phase is modeled as the average of left and right circulations. Emergent dimers are located on the purple minority spins. The resultant quantum superposition is shown below, with a purple shade illustrating the dimer resonance of the plaquette phase. Colors illustrate the amplitude of each spin component. Bottom: phase diagram of the dimer model given by Eq. (13) on the honeycomb lattice [47].

internal energy for each dimer configuration. An effective Hamiltonian for such a system can be written

$$\mathcal{H}_{\rm eff} = \mu \sum_{\hexagon} \left(|\hexagon\rangle\langle\hexagon| + |\hexagon\rangle\langle\hexagon| \right) - g \sum_{\hexagon} \left(|\hexagon\rangle\langle\hexagon| + |\hexagon\rangle\langle\hexagon| \right), \tag{13}$$

where the sum over $\hexagon$ is over all hexagonal loops containing three dimers, depicted by double links. For $g = 0$ and $\mu < 0$, one finds the classical star phase dimer solid [47,48], and for $\mu > 0$, the columnar phase which maps onto the ferromagnetically ordered phase for both kagome and spin ice [42]. As g increases from zero, the star phase order parameter is progressively reduced from saturation [48] up to a threshold and a discontinuous transition into a small window around $\mu/g = 0$, in which quantum fluctuations favor the plaquette phase (see bottom panel of Fig. 5). In the mapping between quantum spin ice and dimer problems, $\mu < 0$ could be thought of as representing the corrections to the dumbbell model from the long-range interactions, which are characteristic of spin ice materials [49,50] and artificial spin ice [51] as, in classical kagome ice, they also drive the system into the $\sqrt{3}\times\sqrt{3}$ phase at low temperature [22]. In the direct mapping from classical nearest-neighbor models, μ is zero, but it is often left as a renormalizable, free parameter [7].

Neutron scattering data from the spin-P phase are easily interpreted using the fragmentation picture. We again expect the data to separate into independent longitudinal and transverse components and predict that the transverse scattering intensity will be reduced by a factor of 4 compared with scattering from the classical $\sqrt{3}\times\sqrt{3}$ phase. This is confirmed in Fig. 4, where we show calculated neutron scattering data from the spin-P phase for neutrons polarized perpendicular to the scattering plane. The intensity scale is reduced by a factor of 4 compared with Fig. 3, highlighting the relative change in the two intensities. The peak structure is identical for the classical and quantum phases, but the intensity difference can be used as a diagnostic to distinguish between them. For example, in the classical limit for the $\sqrt{3}\times\sqrt{3}$ phase, the intensity of the inner ring of star phase peaks at $h = \frac{2}{3}$, $k = 0$ and symmetry-related points, I_d^s, is four times that of charge ordering peaks at $h = 2$, $k = 0$ and related points, I_m, while in the spin-P phase, the two sets of peaks, I_d^p and I_m, have the same intensity.

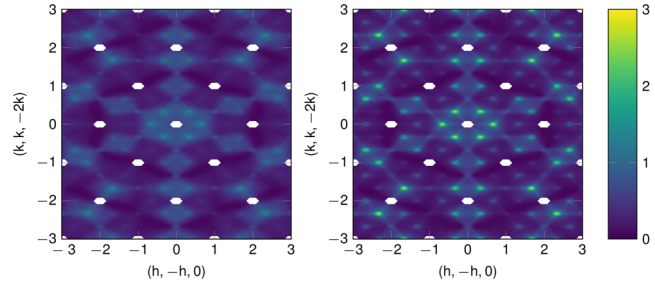

FIG. 6. Unpolarized neutron scattering data in the kagome plane from quantum Monte Carlo simulations of quantum nearest-neighbor spin ice in a [111] field. Left: $\frac{T}{J} = \frac{1}{20}$. Right: $\frac{T}{J} = \frac{1}{320}$. Data are reproduced from Ref. [25] with permission.

This difference could be used as the basis for an order parameter:

$$Q = \sqrt{\frac{4I_m - I_d}{3I_m}}, \tag{14}$$

which distinguishes between the two phases, with $Q = 0$ for the classical $\sqrt{3}\times\sqrt{3}$ ground state and $Q = 1$ for a perfect plaquette phase. This order parameter has the advantage over the one used in quantum Monte Carlo simulations of dimers [48] of being built from experimental observables.

The most recent numerical results suggest that the star-to-plaquette quantum phase transition is first order [48]. As a consequence we anticipate that Q will undergo a discontinuous jump at the transition.

VI. QUANTUM SPIN ICE IN A [111] FIELD

In this section we review data from existing work in the context of the fragmentation picture. Shown in Fig. 6 are constructed unpolarized neutron scattering data in the kagome plane from quantum Monte Carlo simulations. The data, for nearest-neighbor quantum spin ice in a [111] field, are reproduced from Ref. [25]. They are taken in the intermediate field region corresponding to the kagome plateau. The right-hand panel shows data taken at $\frac{T}{J} = \frac{1}{20}$, where T is the temperature and J is the coupling constant. It is consistent with Coulomb phase spin liquid behavior, showing correlated diffuse scattering with pinch point features [42,44]. Bragg peaks at the Brillouin zone centers ($h = 2$, $k = 0$, for example) are

masked. In an experiment these would also coincide with the structural Bragg peaks. On the right we show data at much lower temperature, $\frac{T}{J} = \frac{1}{320}$, where the development of order is clearly observed. A different choice of scale along the vertical axis distorts the sixfold symmetry of the scattering pattern, but despite this, one can observe features similar to those shown in Figs. 3 and 4. In particular, sharpening peaks at $h = \frac{2}{3}$, $k = 0$ and symmetry-related points are clearly visible at the lower temperature. These are the first elements of the radial pattern of peaks characteristic of the pinwheel ordering of the emergent dimers. Moving out along one of the spokes of the pattern the characteristic alternation of high and low intensity peaks is visible. Even here a diffuse scattering background remains, due presumably to remnant incoherent or thermal spin fluctuations about the ordered phase. The figures also show additional peaks compared with Figs. 3 and 4. These are due to scattering from the out-of-plane spin components which appear as a consequence of simulating an unpolarized neutron source.

The order parameter Q [Eq. (14)] could be used as a diagnostic tool to distinguish between the classical $\sqrt{3}\times\sqrt{3}$ and quantum spin-P phases. For this, one would need to include and analyze the magnetic peak intensities at the zone centers coming from the harmonic fragment. Projections of the harmonic sector parallel and perpendicular to the kagome planes provide both the three-dimensional ferromagnetic order and the two-dimensional charge order, which can be separated using the analysis of Sec. III. In experiment the total intensity at these points also includes a dominant structural contribution. An independent estimate of this intensity is necessary. This would be subtracted from the total to give the magnetic scattering intensity. However, in the present case of numerical simulation, the simulated intensities could be compared directly with predicted values.

VII. NEUTRON SCATTERING FROM THE MONOPOLE CRYSTAL PHASE OF SPIN ICE

Similar logic involving the fragmentation protocol can be applied to the ordering process out of the partially ordered fragmented monopole crystal phase of spin ice in zero magnetic field [15,26], and this is the subject of this section. In the monopole crystal phase a vertex carrying a south pole (negative charge) takes the form

$$\begin{aligned} M_{IJ} &= [1, 1, 1, -1] \\ &= \left[\tfrac{1}{2}, \tfrac{1}{2}, \tfrac{1}{2}, \tfrac{1}{2}\right]_{\mathbf{m}} + \left[\tfrac{1}{2}, \tfrac{1}{2}, \tfrac{1}{2}, -\tfrac{3}{2}\right]_{\mathbf{d}}, \end{aligned} \tag{15}$$

and the transverse fragment maps onto one of the Z_2 sectors of the emergent field for hard-core dimers on a diamond lattice [27]. In this case, the element carrying the flux of magnitude $(\frac{m}{a})(\frac{3}{2})$, which is the minority spin of either the "three-in–one-out" or the "three-out–one-in" vertex, corresponds to the dimer position. Monopole charge ordering again coexists with an effective classical dimer liquid represented by the transverse spin fragment.

Complete ordering can again be induced either by quantum fluctuations or by classical corrections to the monopole picture. As in the case of kagome ice, adding corrections to the classical monopole picture through the use of the dipolar spin ice Hamiltonian drives the system into the fully ordered phase illustrated in the top panels of Fig. 7 [26], which we refer to as the spin-R phase. The top middle and top right panels show the longitudinal and transverse fragments, respectively. They show that this can be represented as a classical superposition of the "all-spins-in–all spins-out" order from the charges and the emergent field from the phase of ordered dimers, the R phase [52], and that these distinct phases emerge from the two orthogonal spin fragments. The 16-fold degeneracy of the spin-R phase can be divided into two sets of eight states corresponding to the degeneracy of the R phase. The two sets have reversed monopole ordering on the two sublattices of the diamond lattice, each of which is tied to a Z_2 sector of the emergent dimer field.

The calculated unpolarized neutron scattering intensity from the spin-R phase is shown in the bottom panels of Fig. 7 for the $[hh0]$, $[00l]$ plane. They confirm that the scattering decomposes into a fragmented double-q structure with different ordering wave vectors for the longitudinal and transverse parts. The longitudinal fragment shows the characteristic $q = 0$ ordering of the ionic crystal, while the transverse part orders with $\vec{q} = [hhl]$ in units of the reciprocal cubic cell, $\frac{2\pi}{a_c}$, and with $h + l$ being an odd number. The total intensity is again built of the two independent fragments with no interference terms.

Quantum fluctuations can be added to the dimer model via ring exchange flips around closed hexagons for which Hamiltonian (13) can be adapted. This model has been studied both analytically [47,53] and numerically [52]. For large and negative μ, the dimers crystallize into the classical R phase, which maximizes the number of hexagonal loops or plaquettes of dimers (top left panel of Fig. 7). Switching on the off-diagonal term through finite g, the system is driven through a quantum phase transition. In this case the transition is to a quantum dimer liquid rather than to a resonating dimer solid. For $\mu/g = 1$, hexagonal plaquettes become unfavorable, and the system passes discontinuously into a columnar phase [54] with dimers aligned along one of the [111] axes. The full dimer phase diagram is shown in the bottom panel of Fig. 8.

For the monopole crystal, such emergent dimer moves are generated by small transverse spin coupling compared with the nearest-neighbor exchange. Application of degenerate perturbation theory [53] yields a parameter ratio for the effective dimers of $\mu/g = 0$, which is deep in the classical R phase. The critical threshold [47,53] for entry into the quantum dimer liquid is estimated numerically to be $\mu/g \sim 0.7$ [52]. As a consequence, we do not anticipate the appearance of an effective quantum dimer liquid in this system. In addition, as the inclusion of dipolar corrections to the classical monopole model sees the system order into the spin-R phase [26], this would take a putative quantum system, inclusive of dipolar interactions, even further from an emergent dimer liquid phase.

However, if one could push the system into the quantum dimer liquid phase [55], the neutron scattering signature for the emergent field would strongly resemble that of quantum spin ice [7]. The emergent field for the quantum dimers maps to lattice quantum electrodynamics (LQED) [52] with essentially the same structure and the same emergent photons which should show up in the inelastic neutron scattering spectrum. Integrating over the photon bands to give static spin corre-

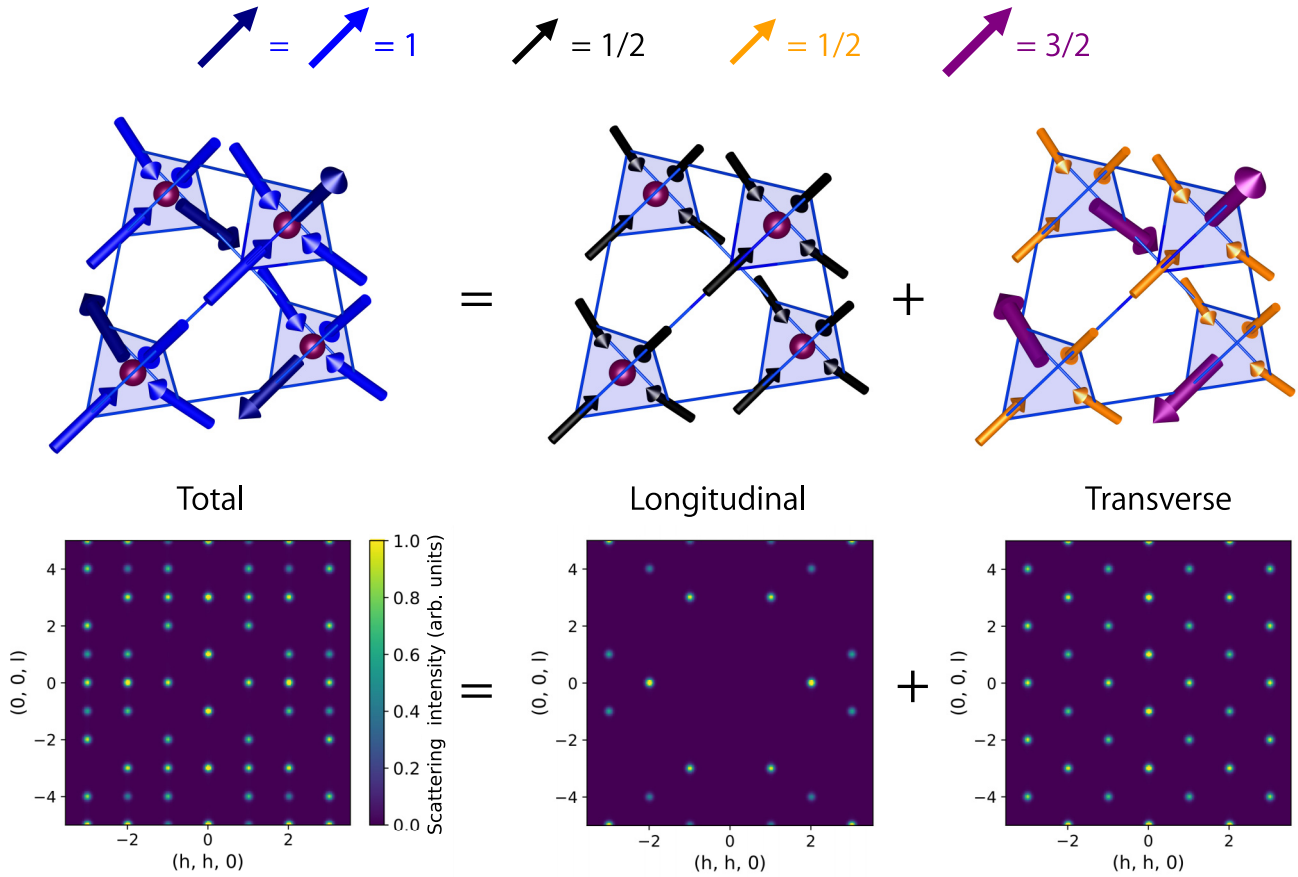

FIG. 7. Top: fragmentation of the spin-R phase magnetic structure—a monopole crystal with ordered transverse fragment. Only half of the tetrahedra are pictured for clarity. Left panel, spin configuration. The minority spins are indicated by a darker shade of blue. Middle panel, longitudinal fragment $\vec{M}_{\mathbf{m}}$ showing "all-spins-in–all-spins-out" ordering. Right panel, transverse fragment $\vec{M}_{\mathbf{d}}$ corresponding to the emergent field for the ordered dimer phase (the R phase; see top panel of Fig. 8). The colors illustrate the amplitude of each spin component. Bottom: unpolarized neutron scattering intensities in the $[hh0]$, $[00l]$ plane computed from the corresponding fragment above. The total scattering picture can also be computed by adding the separate intensities of the two fragments.

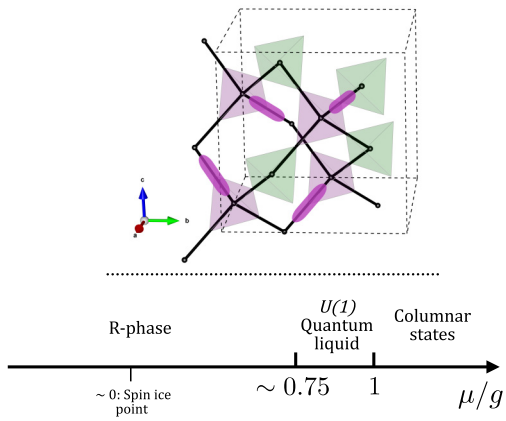

FIG. 8. Top: R-phase dimer structure on the diamond lattice. The tetrahedra shown in Fig. 7 for the spin-R structure are shaded in mauve. The dimer representation is equivalent to the emergent field representation shown in the top right panel of Fig. 7. Bottom: phase diagram [52] for dimers on a diamond lattice as a function of the ratio μ/g from Eq. (13). Also shown is the "spin ice" point corresponding to the location of the monopole crystal plus small transverse quantum spin fluctuations [53], deep within the spin-R phase.

lations, the pinch point structure of the classical system [15] would evolve. The dipolar correlations of the classical system map to correlations in four-dimensional space time with projection onto three dimensions leading to a suppression of the pinch point intensities at the Brillouin zone centers. These predictions could be tested using configurations from the quantum Monte Carlo simulations of Ref. [52] and working backwards to construct the emergent transverse fragment of a monopole crystal. In this partial quantum liquid phase these modified spin correlations from the transverse fragment would coexist with the [220] peaks from the longitudinal fragment or charge order. The intensity of these Bragg peaks should remain unchanged within the regime of emergent quantum dimer fluctuations.

VIII. DISCUSSION

Any vector field can be separated, via a Helmholtz decomposition, into a part with divergence (longitudinal part), a divergence-free part (transverse part), and a harmonic part. In the monopole picture of spin ice and related materials, the magnetic moments play the role of an emergent lattice

field in which such a decomposition or magnetic moment fragmentation is of particular interest. In this description, both ground state and excitation spectrum separate perfectly into elements from the different fragments with well-separated energy scales. The monopoles [2,3] are built from the longitudinal fragment and are high-energy objects, the classical macroscopic degeneracy or quantum photon spectrum come from the transverse fragment, and the topological properties [33,42,44,56] are controlled by the harmonic fragment.

We have shown here that it is extremely useful to carry this decomposition through to the analysis of neutron scattering results, as each component gives a distinct contribution to the neutron scattering intensity. Previous texts have concentrated on situations in which an ordered monopole fragment coexists with the transverse fragment in the form of a correlated spin liquid [15,38,39,43,46]. Here we show that such systems with magnetic charge ordering, when driven into a fully ordered phase, either through quantum fluctuations or by small corrections to the monopole picture, form fragmented double-q structures in which each fragment orders with a distinct ordering wave vector. Due to the separation in energy scales, quantum fluctuations are largely restricted to the transverse fragment. In consequence the intensity reduction of the transverse fragment compared with a known classical limit can be used as a diagnostic tool for the level of quantum fluctuations.

In the specific examples chosen, the KII phase of kagome ice and the monopole crystal of spin ice, the transverse fragment maps onto a Z_2 sector of the emergent field for a hard-core dimer system on hexagonal and diamond lattices, respectively, so that the neutrons indirectly probe dimer solids, both classical and quantum. The analysis we propose relies on the existence of a gapped energy spectrum above the ground state. In this case, the proposed quantum resonances of spins or effective dimers around small closed loops will lead to a quantifiable reduction in the observed neutron scattering intensity. For this to hold, both the temperature scale and the neutron energy resolution must be smaller than this gap.

Bojesen and Onoda [25] have argued that their quantum Monte Carlo data for spin ice in a modest [111] field are consistent with the development of an emergent quantum dimer solid at low temperature. Our paper provides a protocol for a detailed analysis allowing for the distinction between the quantum phase and its classical analog. The energy scale associated with this quantum phase is extremely low—between $1/20$ and $1/320$ of the nearest-neighbor coupling strength—so that quantitative measurement appears to be at the limit of numerical resolution. However, a clearer quantum limit is reached in dedicated quantum dimer simulations on a hexagonal lattice [48]. Our protocol could be tested in detail from such simulations by reconstructing a single Z_2 sector of the emergent field from the dimers and constructing the corresponding neutron scattering plots.

The low energy scales associated with quantum spin ice have so far made identification of experimental systems extremely difficult. One promising example is $Pr_2Hf_2O_7$ [57], which shows some evidence of a quantum spin liquid ground state from inelastic neutron scattering of single-crystal samples. Precision experiments in a [111] field would certainly be of interest here as the first stage in the quest to observe dimensional reduction to the two-dimensional quantum phases predicted in Ref. [25] and discussed in detail above. The stacked kagome layer material $Ho_3Mg_2Sb_3O_{14}$ appears to show quantum corrections to a classical fragmented magnetic structure closely related to the KII phase of kagome ice [58], although for the moment only powder samples exist and the synthesis of pure samples appears challenging. In the absence of single crystals, our analysis could be extended to treat a powder sample. This would be of interest as the signal from the quantum spin-P phase introduced above would be distinct from the alternative quantum phases predicted by Dun *et al.* [58]. However, at least in the short term, artificial systems, such as cold-atom ice fabricated from Rydberg atoms [59], could hold the advantage over materials and could provide promising options for the observation of tunable quantum fluctuations in systems with ice geometry.

Looking forward, open questions remain for the thermal-to-quantum crossover for the phase transitions from ordered to spin liquid phases. In two dimensions in the $g = 0$ limit of Eq. (13), the thermal phase transition from the $\sqrt{3}\times\sqrt{3}$ phase to the KII phase should map to a roughening transition and hence be of Kosterlitz-Thouless type [60], although this could change in the presence of monopole defects [22,23]. As quantum fluctuations are switched on, the fate of the topological transition is far from clear and open to further studies. In three dimensions an evolution of tricritical form is predicted, taking the thermal R-phase-to-dimer-liquid transition from topological to first order as quantum fluctuations increase [53]. In the context of this paper, the ultimate goal would be to prepare experimental signatures of these subtle questions through use of the fragmentation picture in the neutron scattering analysis.

As a final note, the more mathematically inclined reader will notice that the Helmholtz decomposition can be expanded further with regard to the transverse term. Any divergence-free vector field can be decomposed into toroidal and poloidal fields:

$$\begin{aligned}\nabla\times\vec{A} &= \vec{T} + \vec{P} \\ &= \nabla\phi\times\hat{r} + \nabla\times(\nabla\chi\times\hat{r}),\end{aligned} \tag{16}$$

where $\hat{r}$ is a radial unit vector, ϕ is the toroidal scalar potential, and χ is the poloidal scalar potential. Together with the longitudinal potential Ψ, they make up the Debye potentials and allow the mapping of any vector field onto a set of three scalar fields, up to a harmonic contribution [61,62]. The fields from a single point dipole are purely poloidal, while toroidal fields are characteristic of circular solenoids or toroids. The complete decomposition of the transverse magnetic fragment into poloidal and toroidal elements is beyond the scope of this discussion, but pragmatically, one can assume that the extensive loop network leading to pinch point scattering patterns is due largely to the poloidal component, while short loops contain a toroidal contribution. In modified spin ice models with induced attractive interactions between monopoles of like charge, low-energy excitations include like-charge clusters characterized by loops of spin flips, identified as toroidal loops [63–65]. Using the fragmentation picture, it is straightforward to show that such clusters lead to isolated loops in

the transverse fragment, which indeed correspond to a pure toroidal contribution. In a spin liquid phase dominated by such loops, the diffuse neutron scattering is characterized by half-moons of high-intensity straddling the Brillouin zone center, rather than the pinch points of the Coulomb phase. This strongly suggests that magnetic moment fragmentation could be an essential tool for a complete description of such systems.

ACKNOWLEDGMENTS

We acknowledge financial support from the Agence Nationale de la Recherche under Grant No. ANR-19-CE30-0040. We thank Shigeki Onoda for authorizing the reproduction of our Fig. 6 from Ref. [25], as well as Baptiste Bermond for fruitful discussions.

[1] S. V. Isakov, K. Gregor, R. Moessner, and S. L. Sondhi, Phys. Rev. Lett. **93**, 167204 (2004).
[2] C. Castelnovo, R. Moessner, and S. Sondhi, Nature (London) **451**, 42 (2008).
[3] I. A. Ryzhkin, J. Exp. Theor. Phys. **101**, 481 (2005).
[4] M. J. Harris, S. T. Bramwell, D. F. McMorrow, T. Zeiske, and K. W. Godfrey, Phys. Rev. Lett. **79**, 2554 (1997).
[5] S. T. Bramwell and M. J. Gingras, Science **294**, 1495 (2001).
[6] M. Hermele, M. P. A. Fisher, and L. Balents, Phys. Rev. B **69**, 064404 (2004).
[7] O. Benton, O. Sikora, and N. Shannon, Phys. Rev. B **86**, 075154 (2012).
[8] L. Balents, Nature (London) **464**, 199 (2010).
[9] M. J. P. Gingras and P. A. McClarty, Rep. Prog. Phys. **77**, 056501 (2014).
[10] H. Yan, O. Benton, L. D. C. Jaubert, and N. Shannon, Phys. Rev. Lett. **124**, 127203 (2020).
[11] C. Castelnovo and P. Holdsworth, in *Spin Ice* (Springer, New York, 2021), pp. 143–188.
[12] V. Kaiser, J. Bloxsom, L. Bovo, S. T. Bramwell, P. C. W. Holdsworth, and R. Moessner, Phys. Rev. B **98**, 144413 (2018).
[13] C. Castelnovo, R. Moessner, and S. L. Sondhi, Phys. Rev. B **84**, 144435 (2011).
[14] T. Fennell, P. P. Deen, A. R. Wildes, K. Schmalzl, D. Prabhakaran, A. T. Boothroyd, R. J. Aldus, D. F. McMorrow, and S. T. Bramwell, Science **326**, 415 (2009).
[15] M. E. Brooks-Bartlett, S. T. Banks, L. D. C. Jaubert, A. Harman-Clarke, and P. C. W. Holdsworth, Phys. Rev. X **4**, 011007 (2014).
[16] C. L. Henley, Annu. Rev. Condens. Matter Phys. **1**, 179 (2010).
[17] S. T. Bramwell, Nat. Commun. **8**, 2088 (2017).
[18] H. Bhatia, G. Norgard, V. Pascucci, and P.-T. Bremer, IEEE Trans. Visual. Comput. Graph. **19**, 1386 (2013).
[19] E. Lhotel, L. D. Jaubert, and P. C. Holdsworth, J. Low Temp. Phys. **201**, 710 (2020).
[20] M. Zhitomirsky, M. Gvozdikova, and T. Ziman, Ann. Phys. (Amsterdam) **447**, 169066 (2022).
[21] G. Möller and R. Moessner, Phys. Rev. B **80**, 140409(R) (2009).
[22] G.-W. Chern, P. Mellado, and O. Tchernyshyov, Phys. Rev. Lett. **106**, 207202 (2011).
[23] Y. Wang, S. Humeniuk, and Y. Wan, Phys. Rev. B **101**, 134414 (2020).
[24] K.-H. Wu, Y.-P. Huang, and Y.-J. Kao, Phys. Rev. B **99**, 134440 (2019).
[25] T. A. Bojesen and S. Onoda, Phys. Rev. Lett. **119**, 227204 (2017).
[26] L. D. C. Jaubert, SPIN **05**, 1540005 (2015).
[27] D. A. Huse, W. Krauth, R. Moessner, and S. L. Sondhi, Phys. Rev. Lett. **91**, 167004 (2003).
[28] G. Möller and R. Moessner, Phys. Rev. Lett. **96**, 237202 (2006).
[29] M. F. Faulkner, S. T. Bramwell, and P. C. W. Holdsworth, Phys. Rev. B **91**, 155412 (2015).
[30] D. Slobinsky, L. Pili, and R. A. Borzi, Phys. Rev. B **100**, 020405(R) (2019).
[31] A. C. Maggs and V. Rossetto, Phys. Rev. Lett. **88**, 196402 (2002).
[32] L. D. C. Jaubert, M. J. Harris, T. Fennell, R. G. Melko, S. T. Bramwell, and P. C. W. Holdsworth, Phys. Rev. X **3**, 011014 (2013).
[33] L. D. C. Jaubert, J. T. Chalker, P. C. W. Holdsworth, and R. Moessner, Phys. Rev. Lett. **105**, 087201 (2010).
[34] H. M. Revell, L. R. Yaraskavitch, J. D. Mason, K. A. Ross, H. M. L. Noad, H. A. Dabkowska, B. D. Gaulin, P. Henelius, and J. B. Kycia, Nat. Phys. **9**, 34 (2013).
[35] P. C. Guruciaga, S. A. Grigera, and R. A. Borzi, Phys. Rev. B **90**, 184423 (2014).
[36] V. Raban, C. T. Suen, L. Berthier, and P. C. W. Holdsworth, Phys. Rev. B **99**, 224425 (2019).
[37] R. A. Borzi, D. Slobinsky, and S. A. Grigera, Phys. Rev. Lett. **111**, 147204 (2013).
[38] E. Lefrançois, V. Cathelin, E. Lhotel, J. Robert, P. Lejay, C. V. Colin, B. Canals, F. Damay, J. Ollivier, B. Fåk, L. C. Chapon, R. Ballou, and V. Simonet, Nat. Commun. **8**, 209 (2017).
[39] V. Cathelin, E. Lefrançois, J. Robert, P. C. Guruciaga, C. Paulsen, D. Prabhakaran, P. Lejay, F. Damay, J. Ollivier, B. Fåk, L. C. Chapon, R. Ballou, V. Simonet, P. C. W. Holdsworth, and E. Lhotel, Phys. Rev. Res. **2**, 032073(R) (2020).
[40] M. J. Pearce, K. Götze, A. Szabó, T. S. Sikkenk, M. R. Lees, A. T. Boothroyd, D. Prabhakaran, C. Castelnovo, and P. A. Goddard, Nat. Commun. **13**, 444 (2022).
[41] S. V. Isakov, K. S. Raman, R. Moessner, and S. L. Sondhi, Phys. Rev. B **70**, 104418 (2004).
[42] R. Moessner and S. L. Sondhi, Phys. Rev. B **68**, 064411 (2003).
[43] B. Canals, I.-A. Chioar, V.-D. Nguyen, M. Hehn, D. Lacour, F. Montaigne, A. Locatelli, T. O. Menteş, B. Santos Burgos, and N. Rougemaille, Nat. Commun. **7**, 11446 (2016).
[44] A. A. Turrini, A. Harman-Clarke, G. Haeseler, T. Fennell, I. G. Wood, P. Henelius, S. T. Bramwell, and P. C. W. Holdsworth, Phys. Rev. B **105**, 094403 (2022).
[45] P. Fulde, K. Penc, and N. Shannon, Ann. Phys. (Berlin) **514**, 892 (2002).
[46] J. A. M. Paddison, H. S. Ong, J. O. Hamp, P. Mukherjee, X. Bai, M. G. Tucker, N. P. Butch, C. Castelnovo, M. Mourigal, and S. E. Dutton, Nat. Commun. **7**, 13842 (2016).
[47] R. Moessner and S. L. Sondhi, Phys. Rev. B **63**, 224401 (2001).
[48] T. M. Schlittler, R. Mosseri, and T. Barthel, Phys. Rev. B **96**, 195142 (2017).

[49] B. C. den Hertog and M. J. P. Gingras, Phys. Rev. Lett. **84**, 3430 (2000).
[50] S. V. Isakov, R. Moessner, and S. L. Sondhi, Phys. Rev. Lett. **95**, 217201 (2005).
[51] C. Nisoli, R. Moessner, and P. Schiffer, Rev. Mod. Phys. **85**, 1473 (2013).
[52] O. Sikora, N. Shannon, F. Pollmann, K. Penc, and P. Fulde, Phys. Rev. B **84**, 115129 (2011).
[53] D. L. Bergman, G. A. Fiete, and L. Balents, Phys. Rev. B **73**, 134402 (2006).
[54] Referred to as isolated states in Ref. [52].
[55] S. D. Pace, C. Castelnovo, and C. R. Laumann, Phys. Rev. Lett. **130**, 076701 (2023).
[56] L. Pili, A. Steppke, M. E. Barber, F. Jerzembeck, C. W. Hicks, P. C. Guruciaga, D. Prabhakaran, R. Moessner, A. P. Mackenzie, S. A. Grigera, and R. A. Borzi, Phys. Rev. B **105**, 184422 (2022).
[57] R. Sibille, N. Gauthier, H. Yan, M. Ciomaga Hatnean, J. Ollivier, B. Winn, U. Filges, G. Balakrishnan, M. Kenzelmann, N. Shannon, and T. Fennell, Nat. Phys. **14**, 711 (2018).
[58] Z. Dun, X. Bai, J. A. M. Paddison, E. Hollingworth, N. P. Butch, C. D. Cruz, M. B. Stone, T. Hong, F. Demmel, M. Mourigal, and H. Zhou, Phys. Rev. X **10**, 031069 (2020).
[59] A. W. Glaetzle, M. Dalmonte, R. Nath, I. Rousochatzakis, R. Moessner, and P. Zoller, Phys. Rev. X **4**, 041037 (2014).
[60] F. Alet, Y. Ikhlef, J. L. Jacobsen, G. Misguich, and V. Pasquier, Phys. Rev. E **74**, 041124 (2006).
[61] V. M. Dubovik and V. V. Tugushev, Phys. Rep. **187**, 145 (1990).
[62] N. A. Spaldin, M. Fiebig, and M. Mostovoy, J. Phys.: Condens. Matter **20**, 434203 (2008).
[63] M. Udagawa, L. D. C. Jaubert, C. Castelnovo, and R. Moessner, Phys. Rev. B **94**, 104416 (2016).
[64] T. Mizoguchi, L. D. C. Jaubert, R. Moessner, and M. Udagawa, Phys. Rev. B **98**, 144446 (2018).
[65] D. Kiese, F. Ferrari, N. Astrakhantsev, N. Niggemann, P. Ghosh, T. Müller, R. Thomale, T. Neupert, J. Reuther, M. J. P. Gingras, S. Trebst, and Y. Iqbal, Phys. Rev. Res. **5**, L012025 (2023).